GEOPHYSICS, VOL. 86, NO. 1 (JANUARY-FEBRUARY 2021); P. S17–S28, 20 FIGS.
10.1190/GEO2020-0129.1

Least-squares Gaussian beam migration in viscoacoustic media

Yubo Yue[1], Yujin Liu[2], Yaonan Li[3], and Yunyan Shi[4]

ABSTRACT

Because of amplitude decay and phase dispersion of seismic waves, conventional migrations are insufficient to produce satisfactory images using data observed in highly attenuative geologic environments. We have developed a least-squares Gaussian beam migration method for viscoacoustic data imaging, which can not only compensate for amplitude decay and phase dispersion caused by attenuation, but it can also improve image resolution and amplitude fidelity through linearized least-squares inversion. We represent the viscoacoustic Green's function by a summation of Gaussian beams, in which an attenuation traveltime is incorporated to simulate or compensate for attenuation effects. Based on the beam representation of the Green's function, we construct the viscoacoustic Born forward modeling and adjoint migration operators, which can be effectively evaluated by a time-domain approach based on a filter-bank technique. With the constructed operators, we formulate a least-squares migration scheme to iteratively solve for the optimal image. Numerical tests on synthetic and field data sets demonstrate that our method can effectively compensate for the attenuation effects and produce images with higher resolution and more balanced amplitudes than images from acoustic least-squares Gaussian beam migration.

INTRODUCTION

Anelastic properties of a subsurface medium cause amplitude decay and phase dispersion of seismic wavefields, which inevitably lead to poor images with incorrect kinematic and dynamic information, especially in highly attenuative geologic environments. To ensure an accurate recovery of subsurface reflectivity, the quality factor (Q), which is commonly used to quantify attenuation effects (Aki and Richards, 1980), needs to be taken into account during seismic data processing.

Early attempts to mitigate the attenuation effects have applied an inverse Q filtering to the prestack records (Bickel and Natarajan, 1985; Hargreaves and Calvert, 1991; Wang, 2002). However, this method is based on wave back propagation in 1D Q models, so it is inaccurate when handling spatial-variant attenuation in areas with geologic complexity. Nonstationary deconvolution (Margrave et al., 2003, 2011) is another widely used method to perform attenuation compensation, in which nonstationary wavelets are extracted and then used for deconvolution. However, it is challenging to accurately estimate time-variant and frequency-dependent wavelets, especially for data with a low signal-to-noise ratio (Van der Baan, 2012).

Because wavefield attenuation occurs during the wave propagation process, it is natural and physically more accurate to correct for attenuation effects in prestack depth migration (Xie et al., 2009; Zhang et al., 2010; Valenciano et al., 2011; Zhu et al., 2014). Ray-based migrations (Xie et al., 2009; Xin and Hung, 2009; Bai et al., 2016) can be generalized to viscoacoustic media by incorporating an attenuation traveltime, which are integrated along rays traced in the spatial-variant Q model. One-way wave-equation migrations are commonly implemented in the frequency domain, in which amplitude and phase corrections can be implemented by reversing the imaginary part of the complex-valued velocity during the extrapolation of receiver wavefields (Mittet et al., 1995; Yu et al., 2002; Zhang and Wapenaar, 2002; Mittet, 2007; Zhang et al., 2013). Incorporating attenuation compensation into reverse time migration (RTM) can be implemented using different rheological models, including the standard linear solid model (Carcione, 2007; Deng and McMechan, 2008) and the constant-Q model (Zhang et al., 2010; Zhu and Harris, 2014; Zhu et al., 2014). Yang and Zhu (2018) derive a viscoacoustic RTM using a complex-valued time-domain viscoacoustic wave equation.

Conventional migration methods are commonly regarded as the adjoint operators of forward modeling rather than the inverse

Manuscript received by the Editor 28 February 2020; revised manuscript received 2 June 2020; published ahead of production 4 October 2020; published online 16 December 2020.

[1]R&D Center, Bureau of Geophysical Prospecting Inc., Zhuozhou 072751, China. E-mail: geoyyb@163.com.
[2]Beijing Research Center, Aramco Asia, Beijing 100102, China. E-mail: yujin.liu@aramcoasia.com (corresponding author).
[3]China Academy of Railway Sciences, Infrastructure Inspection Research Institute, Beijing 100081, China. E-mail: li_yaonan@126.com.
[4]Geophysical Research Institute, Bureau of Geophysical Prospecting Inc., Zhuozhou 072751, China. E-mail: 1047265697@qq.com.

operators (Claerbout, 1992). They are usually incapable of producing satisfactory images with high resolution and amplitude fidelity because seismic data are acquired with finite acquisition coverages, band-limited source wavelets, and sometimes uneven subsurface illumination. To mitigate these problems, least-squares migration (LSM), which approximates the inverse operator of forward modeling by iteratively seeking a reflectivity model that best predicts the observed data, has been developed. LSM can be implemented using the Kirchhoff integral (Nemeth et al., 1999; Duquet et al., 2000), one-way wave-equation propagator (Kaplan et al., 2010; Huang and Schuster, 2012), or two-way wave-equation propagator (Dai and Schuster, 2013; Zhang et al., 2015; Chen et al., 2017). Hu et al. (2016), Yang et al. (2018), and Yue et al. (2019a, 2019b) show that LSM also can be effectively implemented in terms of Gaussian beams, providing a competitive alternative to existing LSM methods.

Incorporating attenuation compensation into LSM methods can strengthen our ability to improve the resolution and amplitude fidelity of migration images in viscoacoustic media. Kirchhoff LSM is typically used for migrating viscoacoustic data (Shao et al., 2017; Wu et al., 2017). Although it is efficient and flexible, it suffers from the limitations of the classic ray theory, including the singularity problem at caustics and the inability to image multiarrivals (Gray et al., 2001). Least-squares RTM (LSRTM) is another common choice for viscoacoustic data imaging (Dutta and Schuster, 2014; Sun et al., 2016; Chen et al., 2017; Yang and Zhu, 2019). It is accurate even for complex structures. However, because the computational cost of viscoacoustic LSRTM per iteration is usually more than six times that of a standard acoustic RTM (Dutta and Schuster, 2014; Yang and Zhu, 2019), the expense of a whole LSM inversion is often prohibitively high.

To provide an effective approach of viscoacoustic LSM, we propose a viscoacoustic least-squares Gaussian beam migration (LSGBM) method. We first express the viscoacoustic Green's function by a summation of Gaussian beams (Hill, 2001; Gray and Bleistein, 2009), in which an attenuation traveltime is incorporated to simulate the attenuation effects (Keers et al., 2001). Then, based on the beam representation of the Green's function, we construct the linearized Born modeling and adjoint migration operators, which can be effectively evaluated using a time-domain approach based on a filter-bank technique (Ferber, 2005). Instead of an attenuative migration operator decelerating the convergence rate of LSM (Dutta and Schuster, 2014; Chen et al., 2017), we reverse the sign of the amplitude decay term in the Green's function to achieve an amplitude-compensated migration, and we apply a maximum-limited gain function (Zhang et al., 2013) to stabilize the compensation. With the constructed forward modeling and migration operators, we formulate a least-squares inversion and iteratively solve for the optimal image using preconditioned conjugate gradients (Nemeth et al., 1999). To verify the feasibility and effectiveness of the proposed method, we use synthetic and real examples to show that viscoacoustic LSGBM is capable of compensating for the attenuation effects and producing images with higher resolution and more balanced amplitudes than images from acoustic LSGBM.

METHODS

Viscoacoustic Green's function as a sum of Gaussian beams

Using the correspondence principle (Ben-Menahem and Singh, 1981), we can treat wave propagation in an viscoacoustic medium as propagating through an acoustic medium with a frequency-dependent complex velocity $v_C(\mathbf{x}, \omega)$, which can be expressed in terms of an acoustic velocity $v_0(\mathbf{x})$ and a frequency-independent quality factor Q:

$$v_C(\mathbf{x}, \omega) = v_0(\mathbf{x}) \left[1 + \frac{1}{2} i Q^{-1}(\mathbf{x}) + \frac{1}{\pi} Q^{-1}(\mathbf{x}) \ln \left(\frac{\omega}{\omega_0} \right) \right], \tag{1}$$

where ω_0 is a reference frequency for attenuation-related calculations; if the attenuation is small ($Q^{-1}(\mathbf{x})$ & $Lt; 1$), then the attenuation does not alter the raypaths, but it affects the waveform through a frequency-dependent dissipation function (Keers et al., 2001):

$$D(\mathbf{x}, \mathbf{x}', \omega) = \exp\left[-\frac{\omega \tau_Q(\mathbf{x}, \mathbf{x}')}{2} \right] \exp\left[\frac{i\omega}{\pi} \tau_Q(\mathbf{x}, \mathbf{x}') \ln \frac{\omega}{\omega_0} \right], \tag{2}$$

where the first and the second exponential terms on the right side of equation 2 represent the energy absorption and phase shift, respectively. The term $\tau_Q(\mathbf{x}, \mathbf{x}')$ is an attenuation traveltime integrated along the central ray propagating from $\mathbf{x}'$ to $\mathbf{x}$ (Červený, 2001):

$$\tau_Q(\mathbf{x}, \mathbf{x}') = \int_{\text{ray}} \frac{1}{v_0 Q} ds. \tag{3}$$

Accordingly, we can express the viscoacoustic Green's function in terms of Gaussian beams as

$$\begin{aligned} G(\mathbf{x}, \mathbf{x}', \omega) = {} & \frac{i\omega}{2\pi} \iint \frac{dp_x dp_y}{p_z} [A_R(\mathbf{x}, \mathbf{x}') + i A_I(\mathbf{x}, \mathbf{x}')] \\ & \times \exp\left\{ i\omega \left[\tau_R(\mathbf{x}, \mathbf{x}') + \frac{1}{\pi} \tau_Q(\mathbf{x}, \mathbf{x}') \ln \frac{\omega}{\omega_0} \right] \right\} \\ & \times \exp\left[-\omega \tau_I(\mathbf{x}, \mathbf{x}') - \omega \frac{\tau_Q(\mathbf{x}, \mathbf{x}')}{2} \right], \end{aligned} \tag{4}$$

where $\mathbf{p} = (p_x, p_y, p_z)^T$ is the initial ray parameter of the central ray radiating at the surface; $A_R(\mathbf{x}, \mathbf{x}')$ and $A_I(\mathbf{x}, \mathbf{x}')$ are the real and imaginary parts of the beam amplitudes, respectively; and $\tau_R(\mathbf{x}, \mathbf{x}')$ and $\tau_I(\mathbf{x}, \mathbf{x}')$ are the real and imaginary parts of the beam traveltimes (Hill, 2001; Gray and Bleistein, 2009). Note that, different from the attenuation traveltime that varies only along the central ray, the beam traveltimes, respectively vary away from the central rays through the medium.

To verify the correctness of equation 4, we compare the waveforms of its real and imaginary parts at 20 Hz with that of the exact viscoacoustic Green's function (Carcione et al., 1988) in a viscoacoustic medium with a constant velocity v = 2000 m/s and Q = 40 (see Figure 1). The results show that they have a good agreement in amplitude and phase, confirming the validity of equation 4.

Viscoacoustic Gaussian beam Born modeling

In acoustic media, the Born modeling formula for single scattered waves can be expressed in the frequency domain as (Aki and Richards, 2002)

$$u(\mathbf{x}_r,\mathbf{x}_s,\omega)=\omega^2\int d\mathbf{x}m(\mathbf{x})F(\omega)G(\mathbf{x},\mathbf{x}_s,\omega)G(\mathbf{x},\mathbf{x}_r,\omega), \quad (5)$$

where $u(\mathbf{x}_r,\mathbf{x}_s,\omega)$ represents the modeled pressure wavefields with the source and receiver locations denoted by $\mathbf{x}_s$ and $\mathbf{x}_r$, respectively; $F(\omega)$ is the source spectrum; $m(\mathbf{x})=\delta v(\mathbf{x})/v_0(\mathbf{x})$ is the reflectivity at subsurface scattering point $\mathbf{x}$ due to a velocity perturbation $\delta v(\mathbf{x})$ from the background velocity $v_0(\mathbf{x})$; and $G(\mathbf{x},\mathbf{x}_s,\omega)$ and $G(\mathbf{x},\mathbf{x}_r,\omega)$ are the down- and upgoing Green's functions, respectively. After inserting equation 4 into equation 5 and the derivations in Appendix A, we arrive at the viscoacoustic Gaussian beam Born modeling formula:

$$u(\mathbf{x}_r,\mathbf{x}_s,\omega)=-\Phi\sum_{\mathbf{L}}\iint\frac{dp_{rx}dp_{ry}}{p_{rz}}U(\mathbf{L},\mathbf{x}_s,\mathbf{p}_r,\omega)$$
$$\times\exp\left[-i\omega\mathbf{p}_r\cdot(\mathbf{x}_r-\mathbf{L})-\left|\frac{\omega}{\omega_r}\right|\frac{|\mathbf{x}_r-\mathbf{L}|^2}{2w_0^2}\right], \quad (6)$$

where Φ is a frequency-dependent term defined in equation A-7; $\mathbf{L}$ represents the sparsely sampled beam center locations with spacing $\Delta\mathbf{L}=(\Delta L_x,\Delta L_y)$; and ω_r and w_0 are the beam reference frequency and initial half-width for Gaussian beam propagation (Hill, 1990, 2001; Gray, 2005), respectively. The term $U(\mathbf{L},\mathbf{x}_s,\mathbf{p}_r,\omega)$ is the modeled local plane-wave component at each beam center location, which can be expressed as

$$U(\mathbf{L},\mathbf{x}_s,\mathbf{p}_r,\omega)=\int d\mathbf{x}m(\mathbf{x})F(\omega)\iint\frac{dp_{sx}dp_{sy}}{p_{sz}}$$
$$\times[A_R(\mathbf{L},\mathbf{x}_s)+iA_I(\mathbf{L},\mathbf{x}_s)]$$
$$\times\exp\left\{i\omega\left[\tau_R(\mathbf{L},\mathbf{x}_s)+\frac{1}{\pi}\tau_Q(\mathbf{L},\mathbf{x}_s)\ln\frac{\omega}{\omega_0}\right]\right\}$$
$$\times\exp\left[-\omega\tau_I(\mathbf{L},\mathbf{x}_s)-\omega\frac{\tau_Q(\mathbf{L},\mathbf{x}_s)}{2}\right], \quad (7)$$

where the amplitudes $A_R(\mathbf{L},\mathbf{x}_s)$ and $A_I(\mathbf{L},\mathbf{x}_s)$ and traveltimes $\tau_R(\mathbf{L},\mathbf{x}_s)$, $\tau_I(\mathbf{L},\mathbf{x}_s)$, and $\tau_Q(\mathbf{L},\mathbf{x}_s)$ are defined in equations A-2 to A-4 in Appendix A. Equation 6 is a tapered inverse slant stack that spreads the modeled plane waves in equation 7 from each beam center location to the nearby receiver wavefields. Because the evaluation of equation 7 is the innermost step of viscoacoustic Gaussian beam Born modeling, a time-domain implementation based on a filter-bank technique (Ferber, 2005) is given in the next section to ensure an efficient evaluation.

Time-domain approach based on a filter-bank technique

We apply inverse Fourier transform to equation 7, and we arrive at an equivalent expression in the time domain (the terms in parentheses labeling amplitudes and traveltimes are omitted for simplicity):

$$U(\mathbf{L},\mathbf{x}_s,\mathbf{p}_r,t)=\int d\mathbf{x}m(\mathbf{x})\iint\frac{dp_{sx}dp_{sy}}{p_{sz}}$$
$$\times[A_R\delta(t-\tau_R)\otimes f(t,\tau_I,\tau_Q)$$
$$-A_I\delta(t-\tau_R)\otimes f^H(t,\tau_I,\tau_Q)], \quad (8)$$

where δ is the Dirac delta function, $\otimes$ denotes convolution, and $f(t,\tau_I,\tau_Q)$ is a time-domain wavelet filtered by $\exp[-\omega(\tau_I+\tau_Q/2)]$ and $\exp[i\omega\tau_Q\ln(\omega/\omega_0)/\pi]$,

$$f(t,\tau_I,\tau_Q)=\int F(\omega)\exp\left[-i\omega\left(t-\frac{1}{\pi}\tau_Q\ln\frac{\omega}{\omega_0}\right)\right.$$
$$\left.-\omega\left(\tau_I+\frac{\tau_Q}{2}\right)\right]d\omega, \quad (9)$$

and superscript H denotes the Hilbert transform. It is clear that $f(t,\tau_I,\tau_Q)$ varies with subsurface scattering points, so direct evaluation of equation 8 requires massive convolution operations for all scattering points. Notice in equation 9 that $\exp[-\omega(\tau_I+\tau_Q/2)]$ causes only amplitude decay and $\exp[i\omega\tau_Q\ln(\omega/\omega_0)/\pi]$ causes only

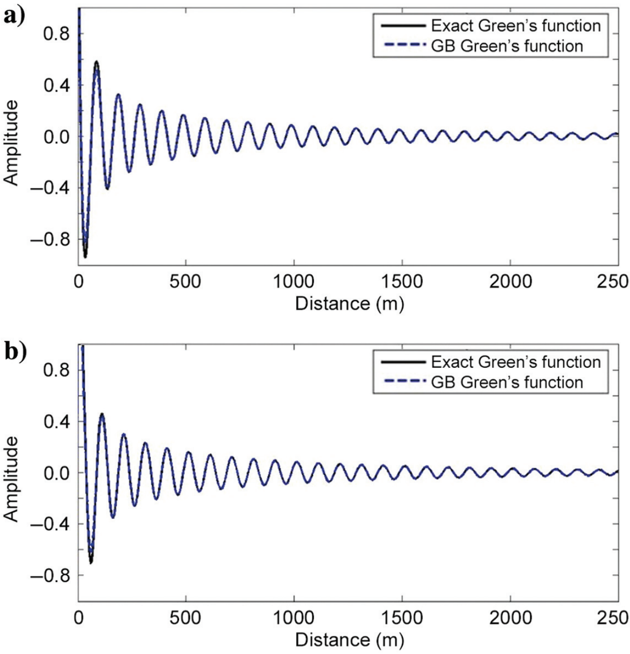

Figure 1. A comparison between the exact Green's function (the solid black line) and the Green's function in terms of Gaussian beams (the dashed blue line) in a viscoacoustic medium with constant v = 2000 m/s and constant Q = 40. (a) Real part comparison and (b) imaginary part comparison between the two Green's functions at 20 Hz.

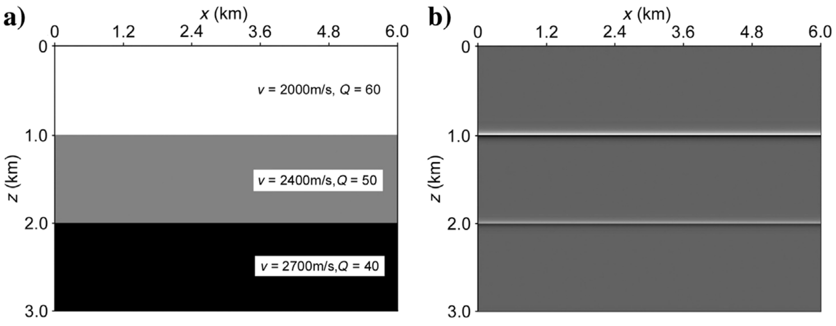

Figure 2. A synthetic plane-layer model. (a) Velocity model and (b) reflectivity.

mild phase shift, so here we can present an approximate evaluation of equation 8 based on the filter-bank technique.

First, we create a 2D bank of the filtered wavelets:

$$\bar{f}(t,\tau_I^j,\tau_Q^k) = \int F(\omega)\exp\left[-i\omega\left(t-\frac{1}{\pi}\tau_Q^k\ln\frac{\omega}{\omega_0}\right) - \omega\left(\tau_I^j+\frac{\tau_Q^k}{2}\right)\right]d\omega, \tag{10}$$

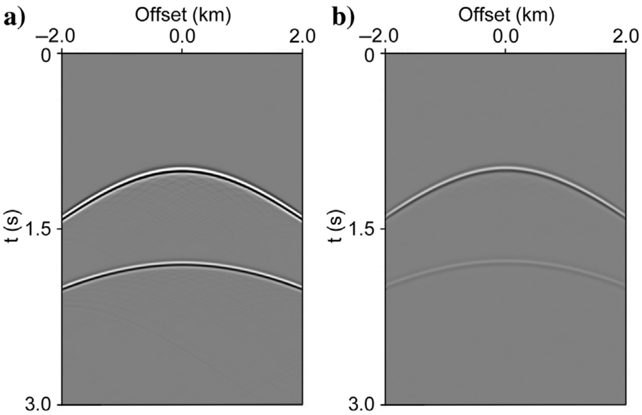

Figure 3. The simulated shot gathers. (a) Nonattenuated data using acoustic Gaussian beam Born modeling and (b) attenuated data using viscoacoustic Gaussian beam Born modeling.

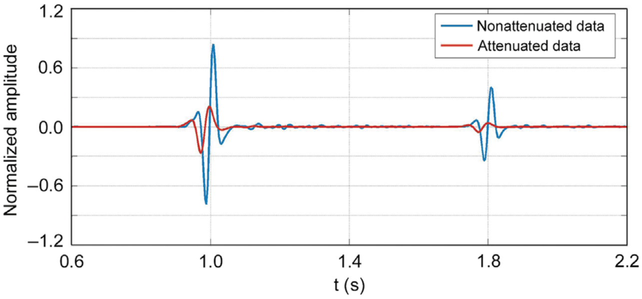

Figure 4. Waveform comparison of the zero-offset trace between nonattenuated data (the blue line) using acoustic Gaussian beam Born modeling and attenuated data (the red line) using viscoacoustic Gaussian beam Born modeling.

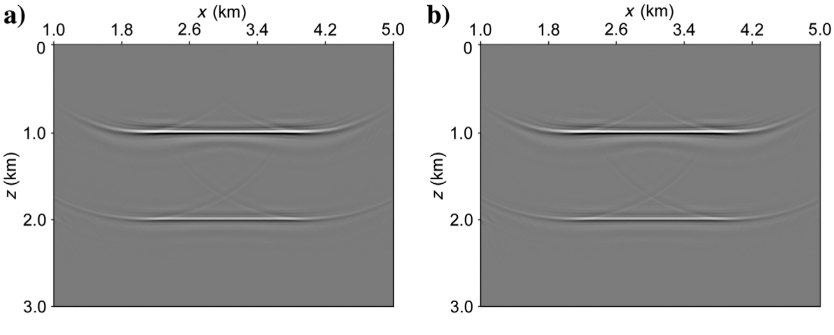

Figure 5. Migration results for the plane-layer model. (a) Acoustic LSGBM image with nonattenuated data and (b) viscoacoustic LSGBM image with attenuated data.

where

$$\begin{aligned} \tau_I^j &= j\Delta\tau_I, \quad 0 \le j < J, \\ \tau_Q^k &= k\Delta\tau_Q, \quad 0 \le k < K, \end{aligned} \tag{11}$$

are discrete samples of τ_I and τ_Q, respectively; J and K are the numbers of samples; and $\Delta\tau_I$ and $\Delta\tau_Q$ are the sampling intervals, respectively. In Appendix B, we discuss the optimal selections of these parameters, which should not only be dense enough to maintain interpolation accuracy, but also be as sparse as possible to keep the total number of filtered wavelets to a minimum.

Then, loop over the source beams in equation 8, and for the scattering points with τ_I and τ_Q satisfying the condition of

$$\begin{aligned} D^{jk}(\mathbf{x}) = \{\mathbf{x}|&(\tau_I^j - \Delta\tau_I \le \tau_I < \tau_I^j + \Delta\tau_I) \\ &\cap (\tau_Q^k - \Delta\tau_Q \le \tau_Q < \tau_Q^k + \Delta\tau_Q)\}, \end{aligned} \tag{12}$$

smear their reflectivity amplitudes to temporary output gathers $R^{jk}(t)$ and $I^{jk}(t)$ using beam amplitudes and traveltimes:

$$\begin{aligned} R^{jk}(t) &= \int_{D^{jk}(\mathbf{x})} m(\mathbf{x})d\mathbf{x} \iint \frac{dp_{sx}dp_{sy}}{p_{sz}} W_I^j W_Q^k A_R \delta(t-\tau_R), \\ I^{jk}(t) &= \int_{D^{jk}(\mathbf{x})} m(\mathbf{x})d\mathbf{x} \iint \frac{dp_{sx}dp_{sy}}{p_{sz}} W_I^j W_Q^k A_I \delta(t-\tau_R), \end{aligned} \tag{13}$$

where $W_I^j = 1 - |\tau_I - \tau_I^j|/\Delta\tau_I$ and $W_Q^k = 1 - |\tau_Q - \tau_Q^k|/\Delta\tau_Q$ are the bilinear interpolation weights.

Finally, we convolve $R^{jk}(t)$ and $I^{jk}(t)$ with the corresponding filtered wavelets $\bar{f}(t,\tau_I^j,\tau_Q^k)$ and $\bar{f}^H(t,\tau_I^j,\tau_Q^k)$, respectively, and then we add the results together to obtain the modeled plane waves:

$$\begin{aligned} U(L,\mathbf{x}_s,\mathbf{p}_r,t) = \sum_{j=0}^{J}\sum_{k=0}^{K}&[\bar{f}(t,\tau_I^j,\tau_Q^k) \\ &\otimes R^{jk}(t) - \bar{f}^H(t,\tau_I^j,\tau_Q^k) \otimes I^{jk}(t)]. \end{aligned} \tag{14}$$

By comparing the computational cost between equations 8 and 14, we can find that the number of smearing operations is comparable but the number of convolution operations of the former is far less than the latter.

Viscoacoustic Gaussian beam migration

Migration is defined as the adjoint operator of forward modeling:

$$\begin{aligned} \hat{m}(\mathbf{x}) = \int d\omega \int d\mathbf{x}_r\omega^2 F^*(\omega)G^*(\mathbf{x},\mathbf{x}_s,\omega) \\ \times G^*(\mathbf{x},\mathbf{x}_r,\omega), \end{aligned} \tag{15}$$

where superscript $*$ denotes complex conjugation. The complex conjugate of equation 4 leads to an anticausal Green's function $G^*(\mathbf{x},\mathbf{x}',\omega)$ that still contains the amplitude decay term $\exp[-\omega\tau_Q(\mathbf{x},\mathbf{x}')/2]$, which not only decreases the resolution of the adjoint migration image, but also decelerates the convergence of LSM (Chen et al., 2017). To compensate for the amplitude decay in migration, we write a modified anticausal Green's function $G^*(\mathbf{x},\mathbf{x}',\omega)$ as

$$\begin{aligned} G^*(\mathbf{x},\mathbf{x}',\omega) = {} & \frac{i\omega}{2\pi}\iint \frac{dp_x dp_y}{p_z}[A_R(\mathbf{x},\mathbf{x}') - iA_I(\mathbf{x},\mathbf{x}')] \\ & \times \exp\left\{-i\omega\left[\tau_R(\mathbf{x},\mathbf{x}') + \frac{1}{\pi}\tau_Q(\mathbf{x},\mathbf{x}')\ln\frac{\omega}{\omega_0}\right]\right\} \\ & \times \exp\left[-\omega\tau_I(\mathbf{x},\mathbf{x}') + \omega\frac{\tau_Q(\mathbf{x},\mathbf{x}')}{2}\right], \end{aligned} \tag{16}$$

by reversing the sign of the amplitude decay term. Using this Green's function in migration allows compensation for the amplitude decay in the recorded data caused by attenuation. After inserting equation 16 into equation 15 and then applying the same strategies as we did in equations A-5 and A-6 to accelerate the migrations, we arrive at the expression of viscoacoustic Gaussian beam migration (GBM):

$$\begin{aligned} \hat{m}(\mathbf{x}) = {} & -\sum_{\mathbf{L}}\iint\frac{dp_{sx}dp_{sy}}{p_{sz}}\iint\frac{dp_{rx}dp_{ry}}{p_{rz}} \\ & \times[A_R S_{\mathbf{L}}(\mathbf{p}_r, t=\tau_R,\tau_I,\tau_Q) + A_I S_{\mathbf{L}}^H(\mathbf{p}_r, t=\tau_R,\tau_I,\tau_Q)], \end{aligned} \tag{17}$$

where $S_{\mathbf{L}}(\mathbf{p}_r,t,\tau_I,\tau_Q)$ is bilinearly interpolated by

$$\begin{aligned} S_{\mathbf{L}}(\mathbf{p}_r,t,\tau_I,\tau_Q) = {} & W_I^j W_Q^k \bar{S}_{\mathbf{L}}(\mathbf{p}_r,t,\tau_I^j,\tau_Q^k) \\ & + W_I^{j+1} W_Q^k \bar{S}_{\mathbf{L}}(\mathbf{p}_r,t,\tau_I^{j+1},\tau_Q^k) \\ & + W_I^j W_Q^{k+1} \bar{S}_{\mathbf{L}}(\mathbf{p}_r,t,\tau_I^j,\tau_Q^{k+1}) \\ & + W_I^{j+1} W_Q^{k+1} \bar{S}_{\mathbf{L}}(\mathbf{p}_r,t,\tau_I^{j+1},\tau_Q^{k+1}), \end{aligned} \tag{18}$$

and $\bar{S}_{\mathbf{L}}$ is a bank of filtered beam components evaluated at discrete τ_I and τ_Q:

$$\begin{aligned} \bar{S}_{\mathbf{L}}(\mathbf{p}_r,t,\tau_I^j,\tau_Q^k) = {} & \Phi\int d\omega F^*(\omega)\int d\mathbf{x}_r u(\mathbf{x}_r,\mathbf{x}_s,\omega) \\ & \times\exp\left[-i\omega[t-\mathbf{p}_r\cdot(\mathbf{x}_r-\mathbf{L})]-\left|\frac{\omega}{\omega_r}\right|\frac{|\mathbf{x}_r-\mathbf{L}|^2}{2w_0^2}\right] \\ & \times\exp\left[-i\omega\frac{1}{\pi}\tau_Q^k\ln\frac{\omega}{\omega_0}-\omega\tau_I^j+\omega\frac{\tau_Q^k}{2}\right]. \end{aligned} \tag{19}$$

To stabilize the amplitude compensation in the evaluation of equation 19, we apply a smooth and maximum-limited gain function proposed by Zhang et al. (2013), in which the amplitude compensation factor $\exp(\omega\tau_Q^k/2)$ is replaced by a gain function $\phi(\eta)$:

$$\phi(\eta) = \begin{cases} \exp(\eta), & \eta \le \ln(G), \\ 1.1G, & \eta > \ln(G)+0.2, \\ G[1-\ln G-2.5(\ln G)^2] \\ +G(1+5\ln G)\eta-2.5G\eta^2, & \text{else}, \end{cases} \tag{20}$$

where $\eta = \omega\tau_Q^k/2$, and G denotes a predefined gain limit. As η increases, the gain function smoothly tends to a constant rather than infinity.

LSM

With the constructed forward modeling and adjoint migration operators, we formulate a viscoacoustic LSGBM scheme to seek the optimal image that best predicts the observed data. The objective function of viscoacoustic LSGBM is defined as

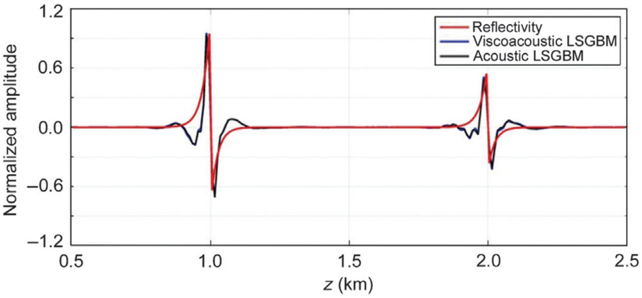

Figure 6. Waveform comparison of traces at $x = 3.0$ among the acoustic LSGBM image using nonattenuated data (the black line), the viscoacoustic LSGBM image using attenuated data (the blue line), and the true reflectivity (the red line).

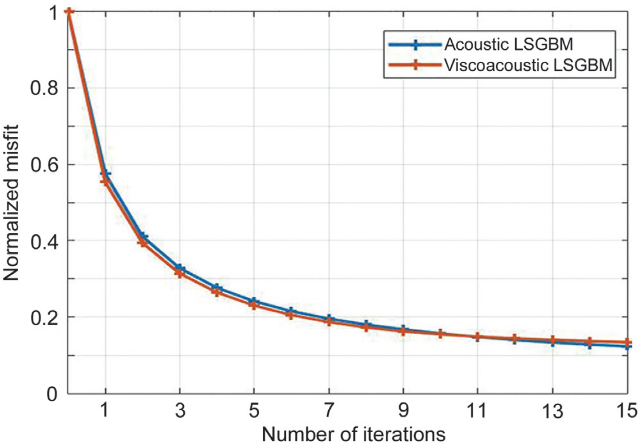

Figure 7. Normalized misfit functions versus iterations for acoustic LSGBM (the blue line) and viscoacoustic LSGBM (the red line).

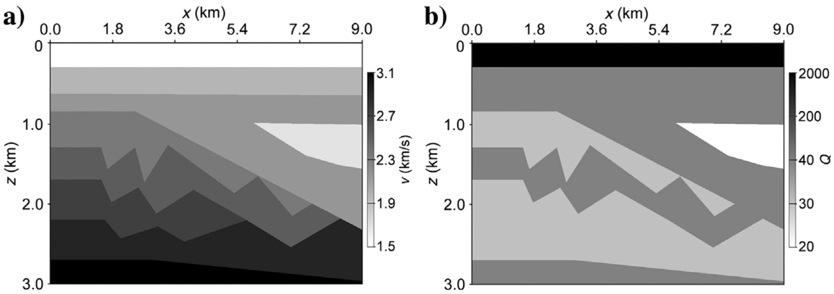

Figure 8. A synthetic multilayer model. (a) Velocity model and (b) Q model.

$$J_0(\mathbf{m}) = \|\mathbf{L}_Q\mathbf{m} - \mathbf{d}_Q\|_2^2 + \mu\|\mathbf{m}\|_2^2, \quad (21)$$

where the first term on the right side of equation 21 is the data misfit function and the second term is a Tikhonov regularization term (Nolet, 1987; Nemeth et al., 1999) that promotes a smooth image, $\mathbf{L}_Q$ is the viscoacoustic Gaussian beam Born modeling operator, $\mathbf{m}$ is the image, $\mathbf{d}_Q$ is the observed data that suffered from attenuation, and μ is a scalar parameter to balance the trade-off between data fitting and smoothing regularization. We use a preconditioned conjugate gradient method (Nemeth et al., 1999) to iteratively solve equation 21, in which the preconditioner is the inverse of diagonal Hessian (Plessix and Mulder, 2004) efficiently evaluated using beam tables (Yang et al., 2018).

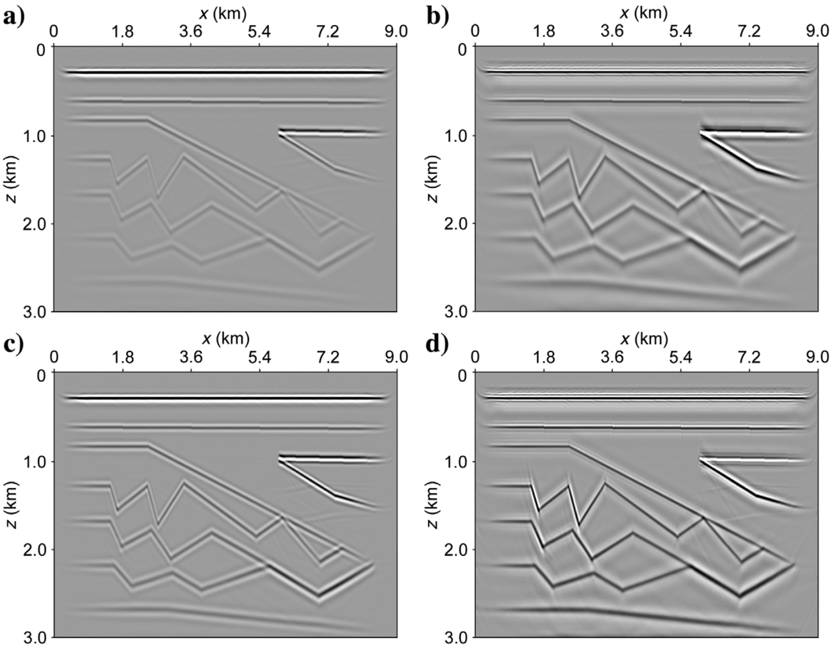

Figure 9. Migration results for the multilayer model. (a) Acoustic GBM image, (b) acoustic LSGBM image, (c) viscoacoustic GBM image, and (d) viscoacoustic LSGBM image.

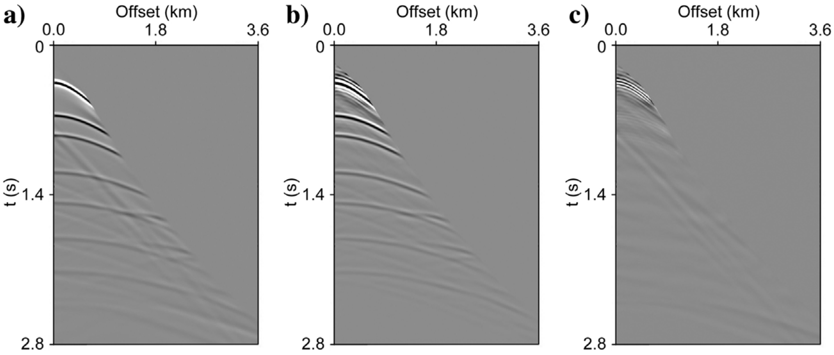

Figure 10. Data comparison (plotted on the same scale) among (a) the observed shot gather, (b) the modeled shot gather using the viscoacoustic LSGBM image shown in Figure 9d, and (c) the data residual between (a) and (b).

NUMERICAL EXAMPLES

The effectiveness of viscoacoustic LSGBM is tested with synthetic and field data examples. The first example is a simple plane-layer model, which is used to demonstrate the ability of viscoacoustic LSGBM to compensate for the attenuation effects contained in attenuated data. The second synthetic and field data examples are used to demonstrate the superiorities of viscoacoustic LSGBM over adjoint GBM and acoustic LSGBM when migrating attenuated data. In the following, acoustic GBM and viscoacoustic GBM refer to the first iteration of acoustic LSGBM and viscoacoustic LSGBM, respectively.

Plane-layer model

A simple plane-layer model is used to test viscoacoustic LSGBM. The model has a grid size of 301 × 301, with lateral spacing of 20 m and vertical spacing of 10 m. The subsurface velocity and Q models are shown in Figure 2a, and the corresponding reflectivity is shown in Figure 2b. An explosive source is placed at $x = 3.0$ km, and 201 receivers are evenly distributed around the source with spacing of 20 m. A Ricker wavelet with 20 Hz peak frequency is used as the source function.

We first use Gaussian beam Born modeling to simulate two types of synthetic shot gather. The nonattenuated data simulated using acoustic Gaussian beam Born modeling (a comparison with the exact acoustic solution can be found in Yue et al., 2019a) are shown in Figure 3a, and the attenuated data simulated using viscoacoustic Gaussian beam Born modeling are shown in Figure 3b. Figure 4 further compares the waveforms of their zero-offset traces. It is evident that the attenuated data show amplitude decay and phase dispersion when compared with the nonattenuated data.

Because adjoint migration is insufficient to recover the true reflectivity with high resolution and amplitude fidelity, we migrate the nonattenuated data using acoustic LSGBM and the attenuated data using viscoacoustic LSGBM. The produced images are shown in Figure 5a and 5b, respectively. We can see that, despite the input data having quite different dynamics characteristics, the produced viscoacoustic LSGBM image is similar to that of acoustic LSGBM, demonstrating a correct attenuation compensation in viscoacoustic LSGBM. The waveforms of both LSGBM images at $x = 3.0$ km along with the true reflectivity are further compared in Figure 6, and the convergence curves of the LSGBM are displayed in Figure 7. We can see that both LSGBM methods achieve a good recovery of the true reflectivity and produce almost identical inversion results at similar convergence rates.

Multilayer model

We use a complex layered model to demonstrate the advantages of viscoacoustic LSGBM over acoustic LSGBM in migrating the attenuated data. Figure 8 shows the velocity model and Q model. The Q values range from 20 to 50, except the first layer with $Q = 2000$. The grid size of the model is 750×750, with lateral spacing of 12 m and vertical spacing of 4 m. A total of 342 single-sided shot gathers are simulated using an O (2,8) time-space-domain finite-difference solver of the viscoacoustic wave equation (Dutta and Schuster, 2014). The shot spacing is 24 m and each shot gather has 300 traces with spacing of 12 m. A zero-phase Ricker wavelet of 20 Hz peak frequency is used in the wavefield simulation and migrations. Figure 10a shows the first shot gather after muting the first arrivals, and we can see that the synthetic data show strong amplitude decay and phase dispersion caused by subsurface attenuation.

Acoustic LSGBM is first applied to the synthetic data. The produced acoustic GBM image and acoustic LSGBM image are shown in Figure 9a and 9b, respectively. Although the acoustic LSGBM image shows improved resolution over the acoustic GBM image in the shallow layers with weak attenuation, both images are blurred in the deeper regions with strong attenuation, in which migration amplitudes are weak and imaging phases are incorrect. We then migrate the data with viscoacoustic LSGBM. The produced viscoacoustic GBM image and viscoacoustic LSGBM image are shown in Figure 9c and 9d, respectively. Compared with the acoustic LSGBM image, the improvements of viscoacoustic LSGBM image are evident in the deeper region with strong attenuation. Not only is the resolution improved, but the migration amplitudes are more balanced as well. Because viscoacoustic LSGBM compensates for the attenuation effects, the correct migration phases in Figure 9c and 9d are also restored. We compare the observed shot gather and the modeled shot gather after viscoacoustic LSGBM, as well as their data residual, in Figure 10. Evidently, the similarity between the observed and the modeled data confirms the good convergence of the data residual in viscoacoustic LSGBM. As shown in Figure 11, viscoacoustic LSGBM also achieves a faster convergence than acoustic LSGBM does. This is because viscoacoustic GBM compensates for the amplitude loss contained in attenuated data and produces a balanced gradient that is closer to the true reflectivity and is thus helpful to accelerate the convergence rate.

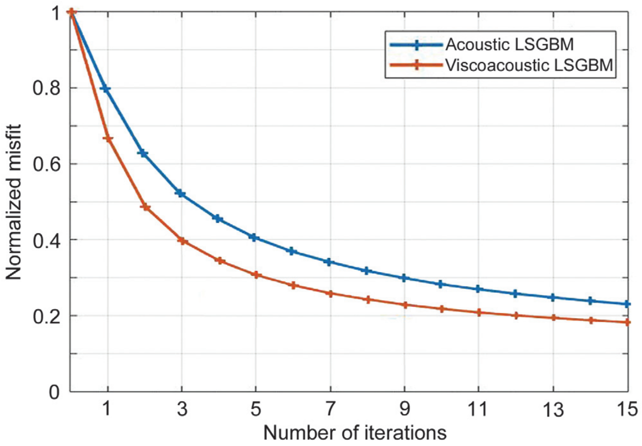

Figure 11. Normalized misfit functions versus iterations for acoustic LSGBM (the blue line) and viscoacoustic LSGBM (the red line).

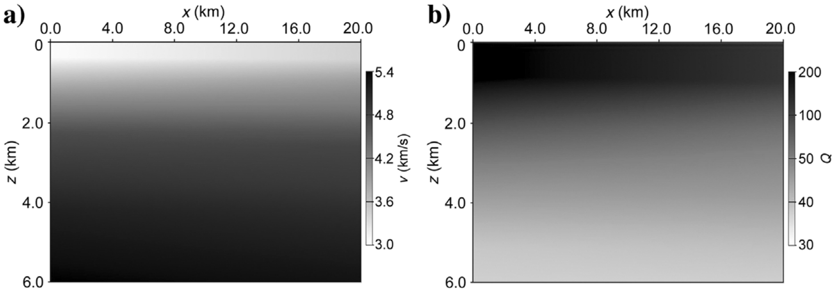

Figure 12. A 2D real data set. (a) Velocity model and (b) Q model.

2D field data

Viscoacoustic LSGBM is finally tested with a 2D real data set. The data set has a total of 262 shot gathers, evenly deployed on the surface with 60 m spacing, and each shot gather has 337 double-sided receivers with 30 m spacing. We have applied a traditional data processing workflow to

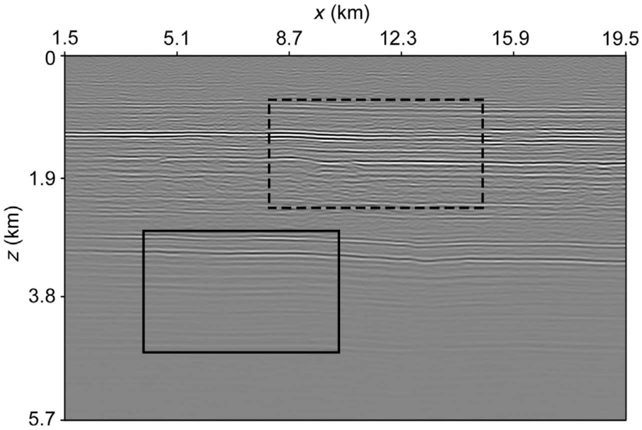

Figure 13. Acoustic Gaussian beam image, where the dotted and solid black boxes indicate the weak and strong attenuated regions used for imaging comparison in Figures 17 and 18, respectively.

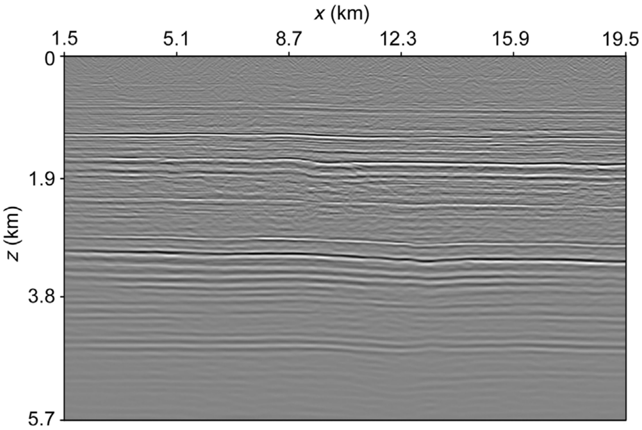

Figure 14. Acoustic least-squares Gaussian beam image.

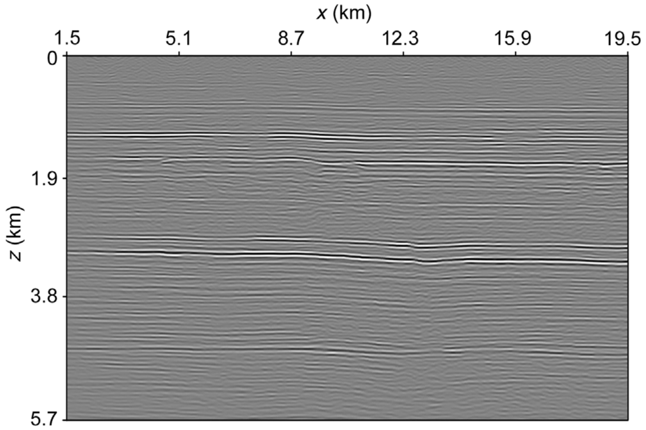

Figure 15. Viscoacoustic GBM image.

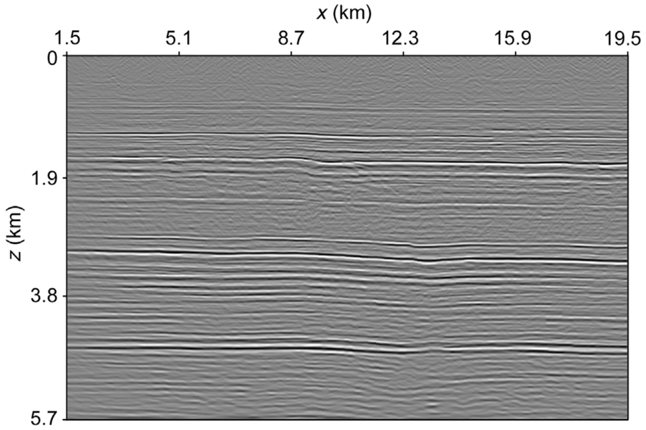

Figure 16. Viscoacoustic LSGBM image.

the recorded data, including a near-surface Q-compensation to alleviate the strong surface-related attenuation effects, which is not taken into account in viscoacoustic LSGBM. Figure 12 shows the velocity model and the Q model obtained by a ray-based Q tomographic inversion (Xin and Hung, 2009). A Ricker wavelet of 25 Hz peak frequency is used in the migration tests.

Eight iterations are required to achieve effective convergence in both LSGBM methods. The data residual decreases approximately 35%–40% for both inversions. The produced acoustic GBM, acoustic LSGBM, viscoacoustic GBM, and viscoacoustic LSGBM images are displayed in Figures 13–16, respectively. It is obvious that viscoacoustic LSGBM achieves optimal images in terms of image resolution and illumination among the four migrations. To make better comparisons among these migration results, we compare all of the images in Figures 17 and 18 for the dotted black and solid black boxes shown in Figure 13, respectively. Similar to the previous example, the acoustic LSGBM image is similar to the viscoacoustic LSGBM image in areas with weak attenuation (Figure 17), and they both have improved resolution (note the events marked by the black arrows) in comparison with the acoustic GBM and viscoacoustic GBM images. However, in areas with strong attenuation (Figure 18), the viscoacoustic LSGBM image is superior to the other images because it not only reveals the thin layers (marked by the black arrows), but it also achieves better structural continuity and improved illumination.

Spectrum comparisons among the magnified views in Figure 18 are shown in Figure 19. We note that viscoacoustic LSGBM and acoustic LSGBM broaden the image bandwidth when compared with their adjoint migrations, whereas the viscoacoustic LSGBM result has higher wavenumber content than the acoustic LSGBM counterpart, which also verifies the enhanced resolution in Figure 18. The observed shot gather, the modeled shot gather after viscoacoustic LSGBM, and their data residual are compared in Figure 20. Evidently, the modeled shot gather is a good prediction of the reflection events in the observed data, whereas the data residual is mainly composed of incoherent noise that cannot be modeled by LSM operators.

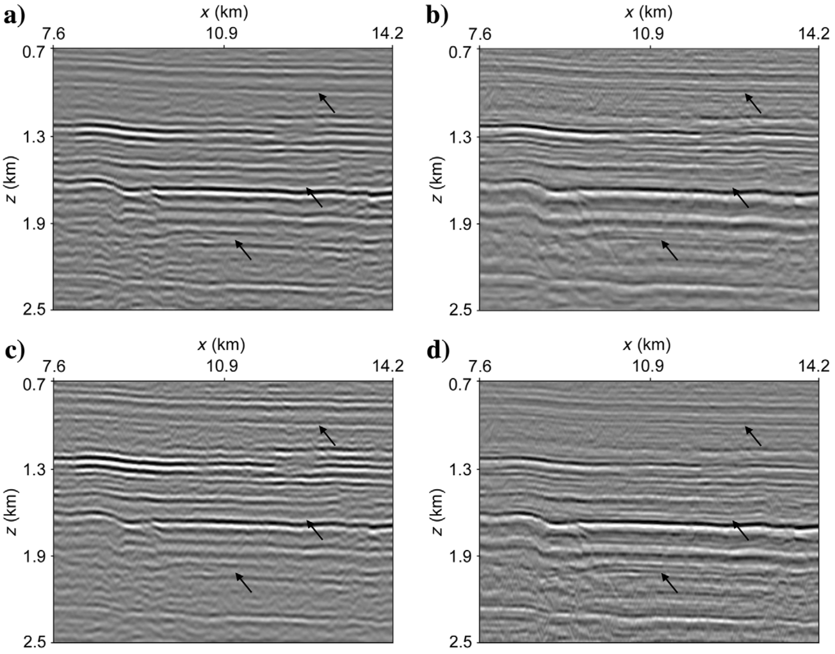

Figure 17. Magnified migration results of the weak attenuated region marked by the dotted black box in Figure 13. (a) Acoustic GBM image, (b) acoustic LSGBM image, (c) viscoacoustic GBM image, and (d) viscoacoustic LSGBM image. Note that the black arrows indicate the events with improved resolution in both LSGBM images compared with those in the adjoint migration images.

DISCUSSION

The GBM is an effective imaging method (Hill, 1990, 2001; Gray, 2005; Gray and Bleistein, 2009; Yue et al., 2012), which has the ability to image multiarrivals while retaining the advantages of ray-based methods. In the previous sections, we have extended this method to linearized least-squares inversion in viscoacoustic media and developed a viscoacoustic LSGBM method to compensate for the attenuation effects contained in attenuated data.

The key to implement viscoacoustic LSGBM is the use of a 2D filter bank that allows us to effectively accommodate attenuation traveltime τ_Q and imaginary beam traveltime τ_I at acceptable costs. In the provided 2D numerical examples with moderate attenuation, viscoacoustic LSGBM requires approximately 30%–50% more computational time than acoustic LSGBM does. As a comparison, the computational cost of viscoacoustic LSRTM is usually two or three times that of standard acoustic LSRTM (Dutta and Schuster, 2014; Yang and Zhu, 2019). However, the direct extension of the filter-bank technique to 3D migrations may cause a memory bottleneck plus a computational burden especially when subsurface attenuation is strong because we have to construct a 5D cube of beam components at each beam center location. One possible way to alleviate this problem is to assign a constant frequency (usually the dominant frequency) for the exponential term in equation 4 that contains the imaginary beam traveltime and controls the amplitude decay off the central ray. This approach only needs to construct a 1D wavelet bank for attenuation traveltime and has limited effects on the overall image quality. Another possible way is to compress the beam components by proper beam compression techniques such as the sparse representation algorithm based on the matching pursuit decomposition proposed by Hu et al. (2015).

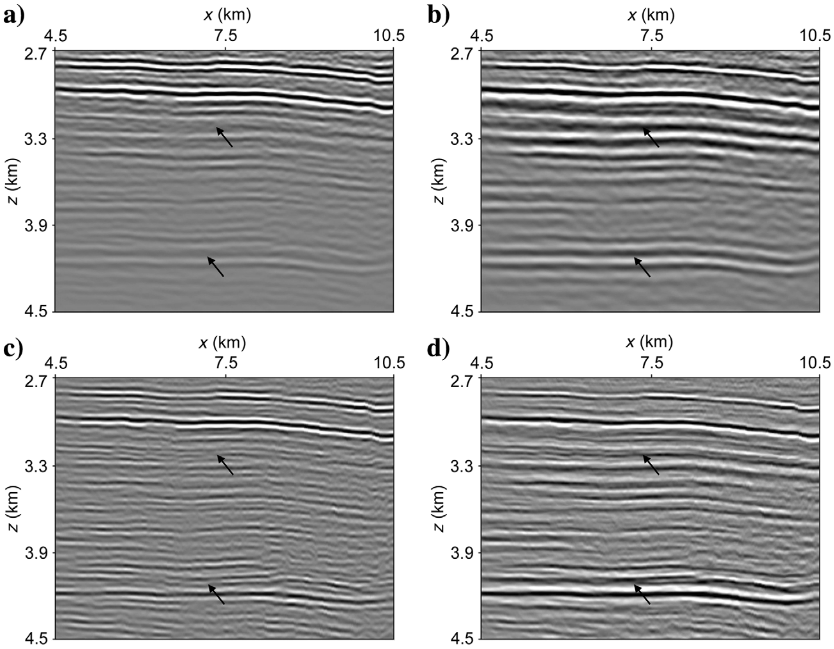

Figure 18. Magnified migration results of the strong attenuated region marked by the solid black box in Figure 13. (a) Acoustic GBM image, (b) acoustic LSGBM image, (c) viscoacoustic GBM image, and (d) viscoacoustic LSGBM image. Note that the events marked by the black arrows in the viscoacoustic LSGBM image have better resolution and structural continuity than those in the other images.

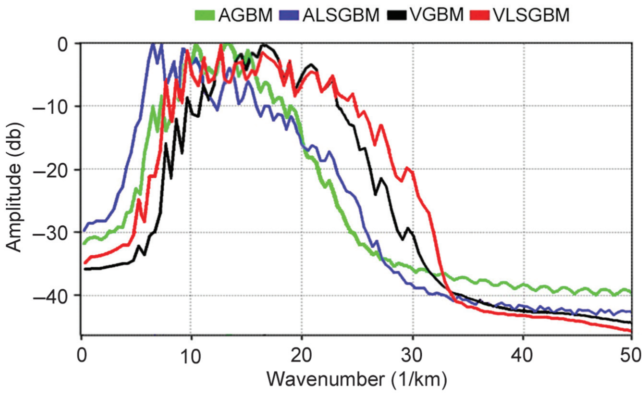

Figure 19. Spectrum comparisons among the migration results shown in Figure 18, where ALSGBM and VLSGBM represent acoustic LSGBM and viscoacoustic LSGBM, respectively, and AGBM and VGBM represent the corresponding adjoint migrations.

The strict adjoint operator of viscoacoustic Born modeling still contains an amplitude decay term that not only decreases the resolution of adjoint migration but also decelerates the convergence of LSM (Dutta and Schuster, 2014; Chen et al., 2017). To avoid this problem, we reverse the sign of the amplitude decay term to introduce an amplitude-compensated GBM. However, this approach induces a stabilization problem that needs careful attention. Perhaps a

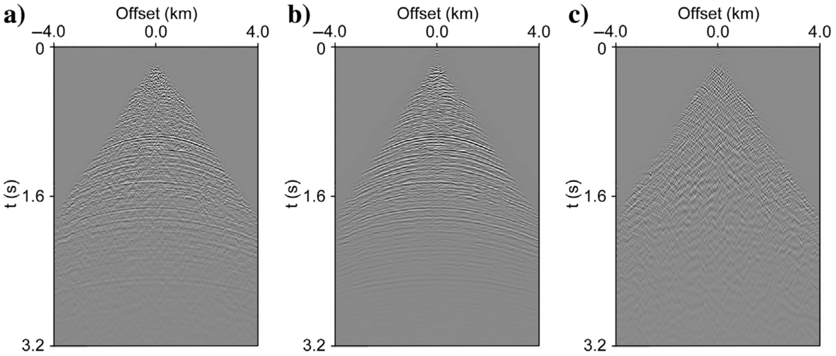

Figure 20. Data comparison (plotted on the same scale) among (a) the observed shot gather, (b) the modeled shot gather after viscoacoustic LSGBM, and (c) the data residual between (a) and (b).

more applicable approach to accelerate the convergence rate is to use a viscoacoustic deblurring filter (Aoki and Schuster, 2009; Chen et al., 2017), which is estimated using point-spread functions constructed by attenuative forward modeling and adjoint migration operators, thus avoiding the instability problem.

CONCLUSION

We have presented a viscoacoustic LSGBM method for imaging attenuated wavefields in viscoacoustic media. By taking the attenuation effects into account in least-squares inversion, this method not only improves imaging resolution and amplitude fidelity, but it also compensates for amplitude decay and phase dispersion caused by attenuation. In addition, by using Gaussian beams as wavefield propagators, this method also achieves a good balance between computational cost and imaging accuracy, both of which are important requirements for iterative LSMs. We have tested the proposed method with 2D synthetic and real data sets. The results show that viscoacoustic LSGBM is capable of producing images with higher resolution and better illumination when compared with adjoint GBM and acoustic LSGBM.

ACKNOWLEDGMENTS

We thank the Bureau of Geophysical Prospecting for permission to publish this paper. We are grateful to J. Shragge (editor in chief), F. Perrone (associate editor), C. Torres-Verdin (assistant editor), S. Gray, H. Hao, and two anonymous reviews for their insightful suggestions and comments. This research was supported by the National Natural Science Foundation of China (grant no. 42074173) and the National Science and Technology Major Project of China (grant no. 2017ZX05018-001).

DATA AND MATERIALS AVAILABILITY

Data associated with this research are available and can be obtained by contacting the corresponding author.

APPENDIX A

VISCOACOUSTIC GAUSSIAN BEAM BORN MODELING

In this appendix, an asymptotic solution for viscoacoustic Born modeling is derived by representing the Green's function as a summation of Gaussian beams.

By inserting equation 4 into equation 5, we can express the viscoacoustic Born modeling formula in terms of beam amplitudes and traveltimes:

$$\begin{aligned}u(\mathbf{x}_r,\mathbf{x}_s,\omega) = &-\frac{\omega^2}{4\pi^2}\int d\mathbf{x}m(\mathbf{x})F(\omega)\\ &\times\iint\frac{dp_{sx}dp_{sy}}{p_{sz}}\iint\frac{dp_{rx}dp_{ry}}{p_{rz}}\\ &\times[A_R(\mathbf{x}_r,\mathbf{x}_s)+iA_I(\mathbf{x}_r,\mathbf{x}_s)]\\ &\times\exp\left\{i\omega\left[\tau_R(\mathbf{x}_r,\mathbf{x}_s)+\frac{1}{\pi}\tau_Q(\mathbf{x}_r,\mathbf{x}_s)\right]\right\}\\ &\times\exp\left[-\omega\tau_I(\mathbf{x}_r,\mathbf{x}_s)-\omega\frac{\tau_Q(\mathbf{x}_r,\mathbf{x}_s)}{2}\right], \qquad \text{(A-1)}\end{aligned}$$

where $A_R(\mathbf{x}_r,\mathbf{x}_s)$ and $A_I(\mathbf{x}_r,\mathbf{x}_s)$ are the real and imaginary parts, respectively, of the product of the source and receiver beam amplitudes,

$$\begin{aligned}A_R(\mathbf{x}_r,\mathbf{x}_s) &= A_R(\mathbf{x},\mathbf{x}_r)A_R(\mathbf{x},\mathbf{x}_s)-A_I(\mathbf{x},\mathbf{x}_r)A_I(\mathbf{x},\mathbf{x}_s),\\ A_I(\mathbf{x}_r,\mathbf{x}_s) &= A_R(\mathbf{x},\mathbf{x}_r)A_I(\mathbf{x},\mathbf{x}_s)+A_I(\mathbf{x},\mathbf{x}_r)A_R(\mathbf{x},\mathbf{x}_s), \quad \text{(A-2)}\end{aligned}$$

$\tau_R(\mathbf{x}_r,\mathbf{x}_s)$ and $\tau_I(\mathbf{x}_r,\mathbf{x}_s)$ are the real and imaginary parts, respectively, of two-way beam traveltimes,

$$\begin{aligned}\tau_R(\mathbf{x}_r,\mathbf{x}_s) &= \tau_R(\mathbf{x},\mathbf{x}_s)+\tau_R(\mathbf{x},\mathbf{x}_r),\\ \tau_I(\mathbf{x}_r,\mathbf{x}_s) &= \tau_I(\mathbf{x},\mathbf{x}_s)+\tau_I(\mathbf{x},\mathbf{x}_r), \qquad \text{(A-3)}\end{aligned}$$

and $\tau_Q(\mathbf{x}_r,\mathbf{x}_s)$ is the two-way attenuation traveltime

$$\tau_Q(\mathbf{x}_r,\mathbf{x}_s) = \tau_Q(\mathbf{x},\mathbf{x}_s)+\tau_Q(\mathbf{x},\mathbf{x}_r). \qquad \text{(A-4)}$$

To accelerate the computation of equation A-1, we first partition the receivers into small regions by applying overlapping Gaussian functions (Hill, 1990; Gray and Bleistein, 2009):

$$\frac{\sqrt{3}}{4\pi}\left|\frac{\omega}{\omega_r}\right|\left(\frac{\Delta L_x\Delta L_y}{w_0}\right)\sum_{\mathbf{L}}\exp\left[-\left|\frac{\omega}{\omega_r}\right|\frac{|\mathbf{x}_r-\mathbf{L}|^2}{2w_0^2}\right]\approx 1; \quad \text{(A-5)}$$

and then we use beams radiating from the center of the regions (beam center $\mathbf{L}$) to approximate the Green's function of the nearby receivers by applying a phase shift $\exp[-i\omega\mathbf{p}_r\cdot(\mathbf{x}_r-\mathbf{L})]$. Then, we arrive at the final 3D Born modeling formula:

$$\begin{aligned}u(\mathbf{x}_r,\mathbf{x}_s,\omega) = &-\Phi\sum_{\mathbf{L}}\iint\frac{dp_{rx}dp_{ry}}{p_{rz}}U(\mathbf{L},\mathbf{x}_s,\mathbf{p}_r,\omega)\\ &\times\exp\left[-i\omega\mathbf{p}_r\cdot(\mathbf{x}_r-\mathbf{L})-\left|\frac{\omega}{\omega_r}\right|\frac{|\mathbf{x}_r-\mathbf{L}|^2}{2w_0^2}\right], \qquad \text{(A-6)}\end{aligned}$$

where

$$\Phi = \frac{\sqrt{3}\omega^4}{16\pi^3}\left|\frac{\omega}{\omega_r}\right|\left(\frac{\Delta L_x\Delta L_y}{w_0}\right), \qquad \text{(A-7)}$$

ΔL_x and ΔL_y are the beam center spacings, and ω_r and w_0 are, respectively, the selected reference frequency and initial half-width of the Gaussian beams (Hill, 1990, 2001). The term $U(\mathbf{L},\mathbf{x}_s,\mathbf{p}_r,\omega)$ is the modeled local plane-wave component:

$$\begin{aligned}U(\mathbf{L},\mathbf{x}_s,\mathbf{p}_r,\omega) = &\int d\mathbf{x}m(\mathbf{x})F(\omega)\iint\frac{dp_{sx}dp_{sy}}{p_{sz}}\\ &\times[A_R(\mathbf{L},\mathbf{x}_s)+iA_I(\mathbf{L},\mathbf{x}_s)]\\ &\times\exp\left\{i\omega\left[\tau_R(\mathbf{L},\mathbf{x}_s)+\frac{1}{\pi}\tau_Q(\mathbf{L},\mathbf{x}_s)\ln\frac{\omega}{\omega_0}\right]\right\}\\ &\times\exp\left[-\omega\tau_I(\mathbf{L},\mathbf{x}_s)-\omega\frac{\tau_Q(\mathbf{L},\mathbf{x}_s)}{2}\right]. \qquad \text{(A-8)}\end{aligned}$$

APPENDIX B

DETERMINING THE OPTIMAL $\Delta\tau_I$ AND $\Delta\tau_Q$

In this appendix, we discuss the determination of the samplings for τ_I and τ_Q. The optimal samplings should not only be dense enough to maintain interpolation accuracy, but also be as sparse as possible to keep the total number of filtered wavelets to a minimum.

The imaginary beam traveltime τ_I in equation 11 causes only amplitude decay of the filtered wavelets, but not phase shift. A common choice for its maximum value and sampling number (Hale, 1992; Yue et al., 2012) is

$$\tau_I^{\mathrm{Max}} = \frac{5}{\omega_r}, J = 10, \tag{B-1}$$

which, in turn, leads to

$$\Delta\tau_I = \frac{0.5}{\omega_r}, \tag{B-2}$$

where the choice of ω_r is usually at the lower end of the seismic data bandwidth.

The attenuation traveltime τ_Q in equation 11 causes an amplitude decay plus a mild phase shift. Because the amplitude decreases monotonically, we focus on the phase variation to determine $\Delta\tau_Q$. In the constructed wavelet bank, the phase variation between two nearby wavelets along the τ_Q axis should at least satisfy the Nyquist criterion to avoid aliasing artifacts:

$$\frac{1}{\pi}\Delta\tau_Q \ln\frac{\omega_{\max}}{\omega_0} \le \frac{\pi}{\omega_{\max}}, \tag{B-3}$$

where $\omega_{\max}$ represents the higher end of the data bandwidth, and ω_0 is the reference frequency in equation 1, which is typically chosen as the dominant frequency. Considering we are using linear interpolation to restore the signal, we halve the sampling interval to ensure accuracy, and then we arrive at

$$\Delta\tau_Q = \frac{\pi^2}{2\omega_{\max}\ln(\omega_{\max}/\omega_0)}. \tag{B-4}$$

Then, we can get the sampling number for τ_Q;

$$J = \frac{\tau_Q^{\mathrm{Max}}}{\Delta\tau_Q}, \tag{B-5}$$

where τ_Q^{Max} is the maximum attenuation travetime, which can be easily obtained during ray tracing.

REFERENCES

Aki, K., and P. G. Richards, 1980, Quantitative seismology: W. H. Freeman & Co.

Aki, K., and P. G. Richards, 2002, Quantitative seismology, 2nd ed.: University Science Books.

Aoki, N., and G. T. Schuster, 2009, Fast least-squares migration with a deblurring filter: Geophysics, **74**, no. 6, WCA83–WCA93, doi: 10.1190/1.3155162.

Bai, M., X. Chen, J. Wu, G. Liu, Y. Chen, H. Chen, and Q. Li, 2016, Q compensated migration by Gaussian beam summation method: Journal of Geophysics and Engineering, **13**, 35–48, doi: 10.1088/1742-2132/13/1/35.

Ben-Menahem, A., and S. J. Singh, 1981, Seismic waves and sources: Springer-Verlag.

Bickel, S. H., and R. R. Natarajan, 1985, Plane-wave Q deconvolution: Geophysics, **50**, 1426–1439, doi: 10.1190/1.1442011.

Carcione, J. M., 2007, Wave fields in real media: Wave propagation in anisotropic, anelastic, porous and electromagnetic media: Elsevier.

Carcione, J. M., D. Kosloff, and R. Kosloff, 1988, Wave propagation simulation in a linear viscoacoustic medium: Geophysical Journal International, **93**, 393–401, doi: 10.1111/j.1365-246X.1988.tb02010.x.

Červený, V., 2001, Seismic ray theory: Cambridge University Press.

Chen, Y., G. Dutta, W. Dai, and G. T. Schuster, 2017, Q-least-squares reverse time migration with viscoacoustic deblurring filters: Geophysics, **82**, no. 6, S425–S438, doi: 10.1190/geo2016-0585.1.

Claerbout, J. F., 1992, Earth soundings analysis: Processing versus inversion: Blackwell Scientific Publications.

Dai, W., and G. T. Schuster, 2013, Plane-wave least-squares reverse-time migration: Geophysics, **78**, no. 4, S165–S177, doi: 10.1190/geo2012-0377.1.

Deng, F., and G. A. McMechan, 2008, Viscoelastic true-amplitude prestack reverse-time depth migration: Geophysics, **73**, no. 4, S143–S155, doi: 10.1190/1.2938083.

Duquet, B., K. J. Marfurt, and J. A. Dellinger, 2000, Kirchhoff modeling, inversion for reflectivity, and subsurface illumination: Geophysics, **65**, 1195–1209, doi: 10.1190/1.1444812.

Dutta, G., and G. T. Schuster, 2014, Attenuation compensation for least squares reverse time migration using the viscoacoustic-wave equation: Geophysics, **79**, no. 6, S251–S262, doi: 10.1190/geo2013-0414.1.

Ferber, R., 2005, A filter bank solution to absorption simulation and compensation: 75th Annual International Meeting, SEG, Expanded Abstracts, 2170–2172, doi: 10.3997/2214-4609-pdb.1.P228.

Gray, S. H., 2005, Gaussian beam migration of common-shot records: Geophysics, **70**, no. 4, S71–S77, doi: 10.1190/1.1988186.

Gray, S. H., and N. Bleistein, 2009, True-amplitude Gaussian-beam migration: Geophysics, **74**, no. 2, S11–S23, doi: 10.1190/1.3052116.

Gray, S. H., J. Etgen, J. Dellinger, and D. Whitmore, 2001, Seismic migration problems and solutions: Geophysics, **66**, 1622–1640, doi: 10.1190/1.1487107.

Hale, D., 1992, Migration by the Kirchhoff, slant stack, and Gaussian beam methods: CWP Report 121, Colorado School of Mines.

Hargreaves, N. D., and A. J. Calvert, 1991, Inverse Q filtering by Fourier transform: Geophysics, **56**, 519–527, doi: 10.1190/1.1443067.

Hill, N. R., 1990, Gaussian beam migration: Geophysics, **55**, 1416–1428, doi: 10.1190/1.1442788.

Hill, N. R., 2001, Prestack Gaussian-beam depth migration: Geophysics, **66**, 1240–1250, doi: 10.1190/1.1487071.

Hu, H., Y. Liu, A. Osen, and Y. Zheng, 2015, Compression of local slant stacks by the estimation of multiple local slopes and the matching pursuit decomposition: Geophysics, **80**, no. 6, WD175–WD187, doi: 10.1190/geo2014-0595.1.

Hu, H., Y. Liu, Y. Zheng, X. Liu, and H. Lu, 2016, Least-squares Gaussian beam migration: Geophysics, **81**, no. 3, S87–S100, doi: 10.1190/geo2015-0328.1.

Huang, Y., and G. T. Schuster, 2012, Multisource least-squares migration of marine streamer and land data with frequency-division encoding: Geophysical Prospecting, **60**, 663–680, doi: 10.1111/j.1365-2478.2012.01086.x.

Kaplan, S. T., P. S. Routh, and M. D. Sacchi, 2010, Derivation of forward and adjoint operators for least-squares shot-profile split-step migration: Geophysics, **75**, no. 6, S225–S235, doi: 10.1190/1.3506146.

Keers, H., D. W. Vasco, and L. R. Johnson, 2001, Viscoacoustic crosswell imaging using asymptotic waveforms: Geophysics, **66**, 861–870, doi: 10.1190/1.1444975.

Margrave, G. F., D. C. Henley, D. C. Lamoureux, M. P. Iliescu, and J. P. Grossman, 2003, Gabor deconvolution revisited: 73rd Annual International Meeting, SEG, Expanded Abstracts, 714–717, doi: 10.1190/1.1818033.

Margrave, G. F., M. P. Lamoureux, and D. C. Henley, 2011, Gabor deconvolution: estimating reflectivity by nonstationary deconvolution of seismic data: Geophysics, **76**, no. 3, W15–W30, doi: 10.1190/1.3560167.

Mittet, R., 2007, A simple design procedure for depth extrapolation operators that compensate for absorption and dispersion: Geophysics, **72**, no. 2, S105–S112, doi: 10.1190/1.2431637.

Mittet, R., R. Sollie, and K. Hokstad, 1995, Prestack depth migration with compensation for absorption and dispersion: Geophysics, **60**, 1485–1494, doi: 10.1190/1.1443882.

Nemeth, T., C. Wu, and G. T. Schuster, 1999, Least-squares migration of incomplete reflection data: Geophysics, **64**, 208–221, doi: 10.1190/1.1444517.

Nolet, G., 1987, Seismic wave propagation and seismic tomography: Springer.

Plessix, R.-E., and W. A. Mulder, 2004, Frequency-domain finite-difference amplitude-preserving migration: Geophysical Journal International, **157**, 975–987, doi: 10.1111/j.1365-246X.2004.02282.x.

Shao, G., D. Zhuang, R. Huang, and P. Wang, 2017, Least-squares Q migration: The path to improved seismic resolution and amplitude fidelity: 87th Annual International Meeting, SEG, Expanded Abstracts, 4400–4404, doi: 10.1190/segam2017-17742644.1.

Sun, J., S. Fomel, T. Zhu, and J. Hu, 2016, Q-compensated least-squares reverse time migration using low-rank one-step wave extrapolation: Geophysics, **81**, no. 4, S271–S279, doi: 10.1190/geo2015-0520.1.

Valenciano, A., N. Chemingui, D. Whitmore, and S. Brandsberg-Dahl, 2011, Wave equation migration with attenuation and anisotropy compensation: 81st Annual International Meeting, SEG, Expanded Abstracts, 232–236, doi: 10.1190/1.3627674.

Van der Baan, M., 2012, Bandwidth enhancement: Inverse Q filtering or time-varying Wiener deconvolution? Geophysics, **77**, no. 4, V133–V142, doi: 10.1190/geo2011-0500.1.

Wang, Y., 2002, A stable and efficient approach of inverse Q filtering: Geophysics, **67**, 657–663, doi: 10.1190/1.1468627.

Wu, X., Y. Wang, Y. Xie, J. Zhou, D. Lin, and C. Lorenzo, 2017, Least square Q-Kirchhoff migration — Implementation and application: 79th Annual Conference and Exhibition, EAGE, Extended Abstracts, 583–588, doi: 10.1071/ASEG2018abW10_1A.

Xie, Y., K. Xin, J. Sun, C. Notfors, A. K. Biswal, and M. K. Balasubramaniam, 2009, 3D prestack depth migration with compensation for frequency dependent absorption and dispersion: 79th Annual International Meeting, SEG, Expanded Abstracts, 2919–2923, doi: 10.3997/2214-4609-pdb.255.52.

Xin, K., and B. Hung, 2009, 3-D tomographic Q inversion for compensating frequency dependent attenuation and dispersion: 79th Annual International Meeting, SEG, Expanded Abstracts, 4014–4018, doi: 10.1190/1.3255707.

Yang, J., and H. Zhu, 2018, Viscoacoustic reverse-time migration using a time-domain complex-valued wave equation: Geophysics, **83**, no. 6, ND1–ND5, doi: 10.1190/geo2018-0050.1.

Yang, J., and H. Zhu, 2019, Viscoacoustic least-squares reverse-time migration using a time-domain complex-valued wave equation: Geophysics, **84**, no. 5, S479–S499, doi: 10.1190/geo2018-0804.1.

Yang, J., H. Zhu, G. McMechan, and Y. Yue, 2018, Time-domain least squares migration using the Gaussian beam summation method: Geophysical Journal International, **214**, 548–572, doi: 10.1093/gji/ggy142.

Yu, Y., R. Lu, and M. D. Deal, 2002, Compensation for the effects of shallow gas attenuation with viscoacoustic wave-equation migration: 72nd Annual International Meeting, SEG, Expanded Abstracts, 2062–2065, doi: 10.1190/1.1817107.

Yue, Y., Z. Li, Z. Qian, J. Zhang, P. Sun, and G. Ma, 2012, Amplitude-preserved Gaussian beam migration under complex topographic conditions: Chinese Journal of Geophysics, **55**, 1376–1383, doi: 10.6038/j.issn.0001-5733.2012.04.033.

Yue, Y., Z. Qian, X. Zhang, D. Wang, Y. Yue, and W. Chang, 2019a, Gaussian beam based Born modeling method for single-scattering waves in acoustic medium: Chinese Journal of Geophysics, **62**, 648–656, doi: 10.6038/cjg2019M0367.

Yue, Y., P. Sava, Z. Qian, J. Yang, and Z. Zou, 2019b, Least-squares Gaussian beam migration in elastic media: Geophysics, **84**, no. 4, S329–S340, doi: 10.1190/geo2018-0391.1.

Zhang, J., and K. Wapenaar, 2002, Wavefield extrapolation and prestack depth migration in anelastic inhomogeneous media: Geophysical Prospecting, **50**, 629–643, doi: 10.1046/j.1365-2478.2002.00342.x.

Zhang, J., J. Wu, and X. Li, 2013, Compensation for absorption and dispersion in prestack migration: An effective Q approach: Geophysics, **78**, no. 1, S1–S14, doi: 10.1190/geo2012-0128.1.

Zhang, Y., L. Duan, and Y. Xie, 2015, A stable and practical implementation of least-squares reverse time migration: Geophysics, **80**, no. 1, V23–V31, doi: 10.1190/geo2013-0461.1.

Zhang, Y., P. Zhang, and H. Zhang, 2010, Compensating for visco-acoustic effects in reverse time migration: 80th Annual International Meeting, SEG, Expanded Abstracts, 3160–3164, doi: 10.1190/1.3513503.

Zhu, T., and J. M. Harris, 2014, Modeling acoustic wave propagation in heterogeneous attenuating media using decoupled fractional Laplacians: Geophysics, **79**, no. 3, T105–T116, doi: 10.1190/geo2013-0245.1.

Zhu, T., J. M. Harris, and B. Biondi, 2014, Q-compensated reverse-time migration: Geophysics, **79**, no. 3, S77–S87, doi: 10.1190/geo2013-0344.1.

Biographies and photographs of the authors are not available.